ASME Journal of Turbomachinery
Online journal at:
https://asmedigitalcollection.asme.org/turbomachinery

Maitri Kshetrimayum
The Stephen B. Klein Faculty of Aerospace Engineering,
Technion—Israel Institute of Technology,
Haifa 3200003, Israel
e-mail: maitri.ksh@campus.technion.ac.il

Beni Cukurel[2]
The Stephen B. Klein Faculty of Aerospace Engineering,
Technion—Israel Institute of Technology,
Haifa 3200003, Israel
e-mail: beni@cukurel.org

Ian Jacobi[2]
The Stephen B. Klein Faculty of Aerospace Engineering,
Technion—Israel Institute of Technology,
Haifa 3200003, Israel
e-mail: ijacobi@technion.ac.il

Compressible Resolvent Analysis for Receptivity and Separation Control in Turbomachinery[1]

Receptivity mechanisms in the separated boundary-layer flow over a high-work-and-lift, low-Reynolds-number airfoil are studied using resolvent analysis. Three-dimensional harmonic forcing is applied to the two-dimensional model airfoil to mimic acoustic excitation, and the corresponding optimal response field is examined. The analysis identifies regions of maximal receptivity and amplification, revealing a convective mechanism in which upstream forcing of wall modes predominantly drives the downstream oscillating shear layer response. Temporal and spatial filters are applied to the resolvent analysis to better simulate physically-realistic excitation fields, and the resulting optimal gain variation with frequency is obtained. Comparisons with matched experimental measurements validate both the receptivity mechanism identification and the gain analysis obtained using the resolvent approach. This study demonstrates that resolvent analysis can predict frequency-dependent disturbance amplification and its impact on experimentally measured lift. Thus, the resolvent technique should be applicable for the future design of high-work-and-lift airfoil geometries. [DOI: 10.1115/1.4072553]

Keywords: separated flows, resolvent analysis, wall modes, acoustic forcing, convective disturbances, flow receptivity, boundary-layer development, computational fluid dynamics (CFD), fluid dynamics in turbine components of gas turbine engines

1 Introduction

High-work low-pressure turbine (LPT) stages are designed to extract substantial enthalpy from the flow while minimizing stage count, weight, and overall engine size. To achieve this, the airfoils in each stage operate at high aerodynamic loading, resulting in significant lift per blade, and often encounter low-Reynolds numbers due to small chord lengths or reduced freestream density at high altitude. Under these conditions, the suction-side boundary layer is predominantly laminar and prone to large separation bubbles, which can fail to reattach under adverse pressure gradients, causing significant aerodynamic losses and reduced efficiency. Consequently, any attempt to increase the lift and work of LPT airfoils must contend with the risk of performance degradation at cruise conditions.

Increasing lift-per-airfoil reduces the number of blades required, while increasing work-per-stage reduces the number of stages. Together these modifications offer substantial reductions in engine weight, length, and cost that are especially important for next-generation unmanned air systems. The LXFHW family of high-lift, high-work airfoils [1] exemplifies this approach, with work and lift coefficients exceeding those of modern GE and P&W E^3 turbine stages. Therefore, this family of airfoils offers significant advantages over the state of the art, if separation and Reynolds-number effects can be effectively managed.

To mitigate these aerodynamic challenges, a variety of active flow-control strategies have been explored to maintain suction-side attachment and efficiency across the low-Reynolds-number regimes typical of high-lift, high-work LPT stages. Techniques such as synthetic jets, pulsed blowing/suction, and plasma-based actuators locally energize the boundary layer near the separation point, thereby delaying or suppressing laminar separation [2–5]. By contrast, acoustic flow control introduces global, traveling-wave perturbations in the freestream, capable of exciting multiple blades simultaneously, including regions inaccessible to localized actuators. Acoustic actuation has demonstrated remarkable overall effectiveness in controlling separated model flows in incompressible wind tunnel flows [6], and follow-up experiments in a transonic linear cascade facility on high-lift, high-work LPT blades [7] have shown measurable improvements in suction pressure and reductions in separated shear-layer angles. Nonetheless, the underlying mechanisms by which acoustic excitation reorganizes the separated flow remain only partially understood.

A key open question concerns causality: do acoustic waves first influence the attached boundary layer and subsequently modify separation, or do they initially reorganize the downstream separation bubble and thereby affect upstream separation? Understanding this causal relationship is critical because it identifies the driving flow structures, informs optimal actuator placement, improves

[1]Paper presented at the Turbo Expo: Turbomachinery Technical Conference & Exposition (GT2026), June 15–19, 2026.
[2]Corresponding authors.

Contributed by International Gas Turbine Institute (IGTI) of ASME for publication in the Journal of Turbomachinery. Manuscript received May 31, 2026; final manuscript received June 23, 2026; published online September 1, 2026. Tech. Editor: David G. Bogard.

energy efficiency, and enables predictive modeling of flow control strategies.

The recent experimental study by Celik et al. [6] sought to resolve this question using phase-averaged particle image velocimetry (PIV) measurements combined with spatio-temporal correlation analysis. They found evidence that the coherent downstream responses in the shear-layer oscillations are driven by upstream wall modes, leading to flow reorganization, a smaller separation bubble, and downstream displacement of the separation point. The study demonstrated that the separation bubble does not drive the flow modifications, nor does the separation point act as the sole driver; rather the upstream wall modes are the primary drivers of the flow reorganization, which means that a small degree of actuation in the upstream wall region can potentially generate large modifications to the separated shear-layer downstream. However, these experiments did not quantify where perturbations are most efficiently amplified in the upstream region, or provide a detailed model to examine how different frequency–wavenumber combinations propagate and contribute to the downstream flow response.

Resolvent analysis addresses these gaps, providing a computationally efficient framework to study receptivity and mode amplification across all relevant frequencies and wavenumbers, at a much lower cost than experiments or full direct numerical simulation (DNS) [8]. Moreover, resolvent analysis provides a framework for predicting the linear response of flows to harmonic forcing and identifying regions most receptive to actuation. A key advantage of this approach is that it requires only the mean flow field as input, which can typically be obtained accurately from Reynolds-averaged Navier–Stokes (RANS) simulations even when fluctuating flow statistics are unavailable. Experimental studies on wall-bounded turbulent flows have verified that resolvent analysis can predict the response modes to mechanical actuation [9,10], demonstrating its value as a design tool for flow control and optimization. Resolvent analysis has also been applied successfully to design active control strategies for separated flows over airfoils [11]. In the current study, a weakly compressible ($M_\infty = 0.05$) version of the resolvent was developed and applied to the low-speed hump representing a high-lift, high-work LPT blade studied previously in experiments by Celik et al. [6]. The compressible resolvent is considerably more challenging than the incompressible case due to the coupling between pressure and density fluctuations, the presence of weak acoustic modes, and increased numerical sensitivity. The resolvent calculations were used to characterize the linear response to harmonic forcing at prescribed frequencies and spanwise wavenumbers, in order to provide a direct computational counterpart to laboratory experiments, and demonstrate the use of the resolvent for the cost-effective development of future airfoil geometries.

Section 2 describes the development of the resolvent for compressible flows. Then in Sec. 3, we show how the resolvent validates previous experimental conclusions about the upstream, wall-mode receptivity of the separated flow. Then we explore how the results of the resolvent calculations are modified by temporal filtering in Sec. 3.2 and spatial filtering in Sec. 3.3. Finally, in Sec. 3.4, we show how physically sensible choices of filtering allow matching the resolvent gain predictions to lift/drag gains obtained experimentally.

2 Methodology

2.1 Governing Equation. The nonlinear compressible Navier–Stokes equations are written for the conserved state vector $\mathbf{q} = [\rho,\ \mathbf{m},\ \mathrm{E}]^T$, where ρ, $\mathbf{m}$, and E are the density, the momentum vector, and the total energy, respectively. The momentum vector is defined as $\mathbf{m} = \rho\mathbf{u} = [\rho u,\ \rho v,\ \rho w]^T$ in the Cartesian streamwise, wall-normal, and spanwise directions. All variables are non-dimensionalized using their freestream values, and the length and time scales used are the hump chord length ($L = 0.116\,\mathrm{m}$) and the eddy turnover time, L/u_∞, respectively. The working fluid is assumed to be a calorically perfect gas (air) with $\gamma = 1.4$ and $\mathrm{Pr} = 0.72$. In the following equations, the variables $\mathbf{u}$, p, T, μ, M_∞, Re are velocity, pressure, temperature, dynamic viscosity, freestream Mach number, and freestream Reynolds number based on chord length; and $\mathbf{I}$ is the identity tensor.

$$\frac{\partial}{\partial t}\begin{bmatrix}\rho\\ \mathbf{m}\\ \mathrm{E}\end{bmatrix} + \begin{bmatrix}\nabla\cdot\mathbf{m}\\ \nabla\cdot(\mathbf{m}\otimes\mathbf{u}) + \frac{1}{\gamma\mathrm{M}_\infty^2}\nabla\cdot p\mathbf{I} - \nabla\cdot\boldsymbol{\tau}\\ \nabla\cdot(\mathrm{H}\mathbf{u} - \Theta)\end{bmatrix} = 0 \tag{1}$$

where

$$\mathrm{E} = \frac{p}{\gamma(\gamma-1)M_\infty^2} + \frac{1}{2}\rho\mathbf{u}\cdot\mathbf{u}, \quad \mathrm{H} = \mathrm{E} + \frac{p}{\gamma\mathrm{M}_\infty^2},$$
$$\boldsymbol{\tau} = \frac{1}{\mathrm{Re}}(\mu(\nabla\otimes\mathbf{u} + (\nabla\otimes\mathbf{u})^T) + \lambda(\nabla\cdot\mathbf{u})\mathbf{I}), \ \ \lambda = -\frac{2}{3}\mu,$$
$$\mu(T) = T^{3/2}\frac{1 + S/T_\infty}{T + S/T_\infty}, \ \ S = 110.4\,\mathrm{K}, \ \ T_\infty = 293.15\,\mathrm{K}$$
$$\Theta = \boldsymbol{\tau}\cdot\mathbf{u} + \frac{\mu}{(\gamma-1)\mathrm{M}_\infty^2\mathrm{RePr}}\nabla T,$$
$$p = \rho T$$

2.2 Baseflow. The steady baseflow $\bar{\mathbf{q}}$ was obtained by solving the RANS equations using the Spalart–Allmaras turbulence model in ANSYS FLUENT with a density-based solver. The solver setup was validated by reproducing the NASA 2D Bump-in-channel case at $\mathrm{M}_\infty = 0.2$ and $\mathrm{Re} = 1\times10^6$ [12], showing very good agreement with the benchmark data of wall skin-friction and pressure coefficients (plots are shown in Appendix A). The validated setup was then used to compute the baseflow for the present study using the LXFHW-LSH-28 hump geometry from Ref. [6] at $\mathrm{M}_\infty = 0.05$ and $\mathrm{Re} \approx 42,700$.

A mesh-independence study was conducted for this configuration, included in Appendix B; the final grid comprised approximately 0.8 million cells with maximum $y^+ \approx 0.7$ at the wall. Pressure far-field boundary conditions were applied at the inlet and outlet, while the wall was modeled as adiabatic and no-slip. The upper boundary, as well as the upstream and downstream extensions of the wall, were treated as symmetry planes. A far-field turbulent viscosity of $0.009\,(\mu_\infty/\rho_\infty)$ was prescribed. This mesh-independent baseflow was used as the input for the resolvent analysis.

2.3 Resolvent Analysis. Resolvent analysis studies the response of small-amplitude perturbations around a steady baseflow, denoted by $\bar{\mathbf{q}}$, which satisfies the nonlinear Navier–Stokes equations (Eq. (1)). Linearizing the equations about this baseflow yields the following semi-discrete system for the perturbations $\mathbf{q}'$:

$$\frac{\partial\mathbf{q}'}{\partial t} + \mathbf{J}\mathbf{q}' = \mathbf{f} \tag{2}$$

$$\boldsymbol{\phi} = C\mathbf{q}' \tag{3}$$

where $\mathbf{J}$ denotes the Jacobian matrix or the linearized Navier–Stokes operator, $\mathbf{q}'$ is the perturbation state vector, and $\mathbf{f} = B\,\mathbf{f}_s$ represents either the nonlinear terms neglected in the linearization or an externally imposed forcing. The matrix B specifies how the input enters into the state equation, while C maps the state vector to the desired output quantity $\boldsymbol{\phi}$. In practice, B and C are diagonal matrices with entries of 0 or 1, where 1 indicates the spatial regions and/or state components relevant for forcing (B) and response (C).

Assuming three-dimensional perturbations that are homogeneous along the spanwise direction and evolve harmonically in time with frequency ω, these perturbations can be expressed as Fourier modes with spanwise wavenumber k_z

$$\mathbf{q}'(x, y, z, t) = \hat{\mathbf{q}}(x, y)\, e^{\mathrm{i}(k_z z - \omega t)} + \mathrm{c.c} \tag{4}$$

$$\mathbf{f}(x, y, z, t) = \hat{\mathbf{f}}(x, y)\, e^{\mathrm{i}(k_z z - \omega t)} + \mathrm{c.c} \tag{5}$$

where c.c. denotes the complex conjugate of the complex state variable modes, leading to the frequency-domain system

$$(-\mathrm{i}\omega \mathbf{I} + \mathbf{J})\hat{\mathbf{q}} = B\hat{\mathbf{f}}_s \tag{6}$$

$$\hat{\boldsymbol{\phi}} = C\hat{\mathbf{q}} \tag{7}$$

In resolvent form, the system can be written as an input–output mapping

$$\hat{\boldsymbol{\phi}} = C\,(-\mathrm{i}\,\omega_r \mathbf{I} + \mathbf{J})^{-1} B\,\hat{\mathbf{f}}_s \tag{8}$$

where ω_r is the (real) temporal frequency used in resolvent analysis and

$$\mathbf{R}(k_z, \omega_r) = (-\mathrm{i}\,\omega_r \mathbf{I} + \mathbf{J})^{-1} \tag{9}$$

is the global resolvent operator. This operator maps the harmonic forcing $\hat{\mathbf{f}}$ to the corresponding flow response $\hat{\boldsymbol{\phi}}$. The optimal gain σ_0 quantifies the maximum amplification from input to output, defined as the largest ratio of the perturbation energy of the response to that of the forcing

$$\sigma_0^2 = \sup_{\hat{\mathbf{f}}} \frac{\|\hat{\boldsymbol{\phi}}\|_E^2}{\|\hat{\mathbf{f}}\|_F^2} \tag{10}$$

Here, $\|\cdot\|_F$ and $\|\cdot\|_E$ denote the energy norms associated with the forcing and response spaces, respectively.

2.4 Numerical Methods. The linearized Navier–Stokes operator $\mathbf{J}$ is spatially discretized using a cell-centered finite-volume framework, following the formulation described by Dwivedi [13]. The same flux discretization strategy is adopted here, and the reader is referred to Ref. [13] for numerical details.

The optimization problem in Eq. (10) is reformulated as a Hermitian eigenvalue problem in Eq. (11)

$$\underbrace{U_F^{-H}(B^H \mathbf{R}^H C^H Q_E C \mathbf{R} B) U_F^{-1}}_{\mathbf{A}}\ \hat{\mathbf{f}}_s = \sigma_0^2\, \hat{\mathbf{f}}_s \tag{11}$$

where $\mathbf{A}$ is a Hermitian matrix. This problem is then solved using a matrix-free Krylov-based algorithm, following the approach of Bugeat et al. [14]. This requires solving a pair of linear systems involving the direct linear operator ($\mathbf{R}^{-1}$) and its adjoint, which is approximated by its Hermitian transpose. The energy norms associated with the discrete scalar products in Eq. (10) are denoted by Q_F and Q_E for the forcing and response fields, respectively. The matrix Q_F is positive definite and derived from the canonical scalar product, and is written in the eigenvalue problem form in Eq. (11) according to

$$B^H Q_F B = U_F^H U_F \tag{12}$$

whereas the incompressible kinetic energy norm is employed for Q_E; the mathematical expression of these matrices are given in Ref. [14]. As noted therein, the absolute value of optimal gain does not correspond to a physically meaningful energy amplification, since $\|\hat{\mathbf{f}}\|_F^2$ is not dimensionally consistent with energy. However, its relative variation across wavenumbers and frequencies remains a valuable indicator of the flow receptivity and is central to resolvent analysis.

In this study, the discretized linear operator was constructed in MATLAB, and the optimization problem was solved using the PETSc library [15]. SLEPc's Krylov–Schur algorithm solved the Hermitian eigenvalue problem, while MUMPS enabled parallel sparse direct LU factorization for the linear systems.

2.5 Numerical Setup. The computational domain for the 2D baseflow used in the resolvent analysis was truncated, as shown in Fig. 1, and a domain truncation study confirmed that the optimal gain is independent of domain size. The mesh, generated using Gmsh, had uniform streamwise spacing and a wall-normal geometric progression factor of 1.02. Mesh and domain independence results are summarized in Table 1. Mesh-G ($N_x = 4320$, $N_y = 300$ grid cells) proved sufficient: wall-normal refinement (Mesh-H) altered optimal gain by only 2%, with negligible effects from domain extent or streamwise spacing. The computations (single-node, shared-memory) were performed on the Technion HPC Cluster (Rocky Linux 8). Each run utilized 60 CPU cores and ~ 850 GB memory, with a wall-clock time of ~ 2.5 h.

Dirichlet boundary conditions are imposed on the perturbations at the inlet, while Neumann boundary conditions are applied at the outlet. The upper boundary, as well as the upstream and downstream extensions of the wall, are treated as symmetry planes, where the normal perturbation vanishes ($v' = 0$) and zero-gradient conditions are imposed on the other variables, i.e., (u', w', T'). The wall itself is treated as adiabatic, with no-slip conditions ($u' = 0$, $v' = 0$, $w' = 0$) and a Neumann condition for temperature.

The forcing was confined to $-0.5 \le x/L \le 11$ and $0 \le y/L \le 1.0$ to isolate physical amplification mechanisms and avoid unrelated numerical artifacts from upstream or the far field, while the response field was unrestricted to capture the full global dynamics. Numerical sponge layers were implemented at the inlet, exit, and top boundaries, with respective extents of $4L$, $5L$, and $4L$, in order to minimize spurious reflections and to ensure the smooth absorption of outgoing disturbances. The results were verified to be independent of the sponge strength. All results discussed here focus on two-dimensional modes, i.e., $k_z = 0$, since they were found to be the most amplified (see Appendix C).

3 Results

3.1 Unfiltered Forcing and Response Behavior. The optimal forcing and response resolvent modes ($\hat{\mathbf{f}}$, $\hat{\boldsymbol{\phi}}$) were computed over a range of non-dimensional frequencies described in terms of a normalized Strouhal number, $\mathrm{St}/\sqrt{\mathrm{Re}}$, to account for the Reynolds-number dependence of the dominant separated-shear-layer dynamics [6]. The forcing and response velocity modes, $\hat{\mathbf{u}}(x, y, \omega, k_z)$, were then obtained, and the two-dimensional distribution of kinetic energy $\tilde{E}'_K(x, y)$ was calculated for a given frequency and wavenumber combination according to

$$\tilde{E}'_K(x, y) = \frac{12\,\bar{\rho}(x, y)\,\|\hat{\mathbf{u}}(x, y, \omega, k_z)\|^2}{\max_{x,y}\left(12\,\bar{\rho}(x, y)\,\|\hat{\mathbf{u}}(x, y, \omega, k_z)\|^2\right)} \tag{13}$$

The top rows of Figs. 2 and 3 show the normalized modal energy fields for the optimal forcing and response as contour plots for two different forcing frequencies, $\mathrm{St}/\sqrt{\mathrm{Re}} = 0.006$ and $\mathrm{St}/\sqrt{\mathrm{Re}} = 0.035$. Darker regions indicate higher energy density. The forcing fields in panel (*a*) highlight the regions where applied disturbances are most effective at exciting the flow, while the response fields in panel (*b*) indicate where the flow responds most strongly to the given forcing.

The bottom rows of Figs. 2 and 3 present the streamwise variation in the wall-normal integrated energy $\tilde{E}'_K(x)$ given by

$$\tilde{E}'_K(x) = \frac{12\int_{y_{\min}}^{y_{\max}} \bar{\rho}(x, y)\,\|\hat{\mathbf{u}}(x, y, \omega, k_z)\|^2\, dy}{\max_x\left(12\int_{y_{\min}}^{y_{\max}} \bar{\rho}(x, y)\,\|\hat{\mathbf{u}}(x, y, \omega, k_z)\|^2\, dy\right)} \tag{14}$$

The wall-normal integration of the full energy map highlights the streamwise locations where the modal forcing and response energy peaks. At low frequencies ($\mathrm{St}/\sqrt{\mathrm{Re}} = 0.006$), the response

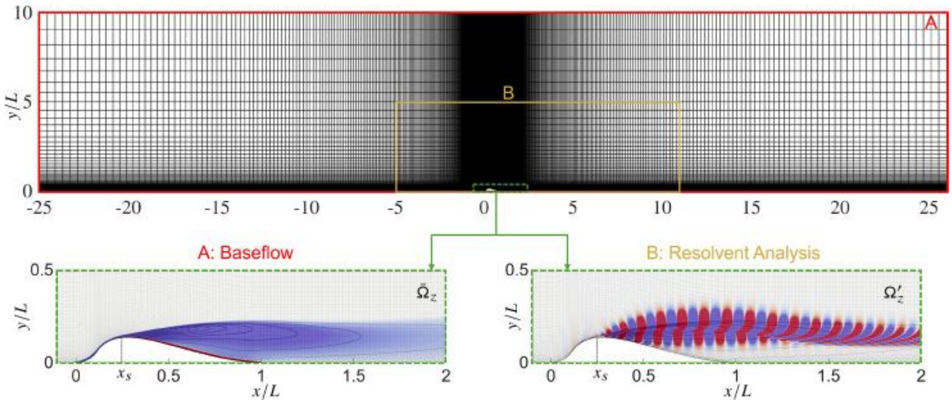

Fig. 1 Computational domain for the baseflow (A) and resolvent analysis (B): (top) every fifth grid point, (bottom) every third grid point; contour plots are overlaid with contour lines of the baseflow vorticity $\bar{\Omega}_z$

Table 1 Mesh and domain independence study for optimal gain at $k_z = 0$ and $\mathrm{St}/\sqrt{\mathrm{Re}} = 0.035$

Mesh	x/L	y/L	N_w	N_y	σ_0^2
A	[−10,21]	[0,5]	100	250	7.282190×10^4
B	[−5,11]	[0,5]	100	250	7.282180×10^4
C	[−5,11]	[0,7]	100	267	7.311120×10^4
D	[−5,11]	[0,5]	250	250	2.612650×10^4
E	[−5,11]	[0,5]	270	250	2.555180×10^4
F	[−5,11]	[0,5]	280	250	2.519080×10^4
G	[−5,11]	[0,5]	270	300	1.947660×10^4
H	[−5,11]	[0,5]	270	310	1.909130×10^4

Note: Here N_w and N_y are the number of cells along the wall boundary and Cartesian y-direction, respectively.

is highly energetic in the wake and extends far downstream, whereas at higher frequencies ($\mathrm{St}/\sqrt{\mathrm{Re}} = 0.035$), the response becomes more localized and shifts closer to the body.

The frequency trends for the forcing and response modes are summarized in Fig. 4, which displays a map of the wall-normal integrated modal energy, $\tilde{E}'_K(x)$ (i.e., the bottom rows of Figs. 2 and 3) over the range of all frequencies to show the streamwise location of the maximal forcing and response as a function of frequency. The energetic peak locations for the two specific frequencies examined in Figs. 2 and 3 are marked by circular and square markers, respectively, in those figures and on the combined map, for reference.

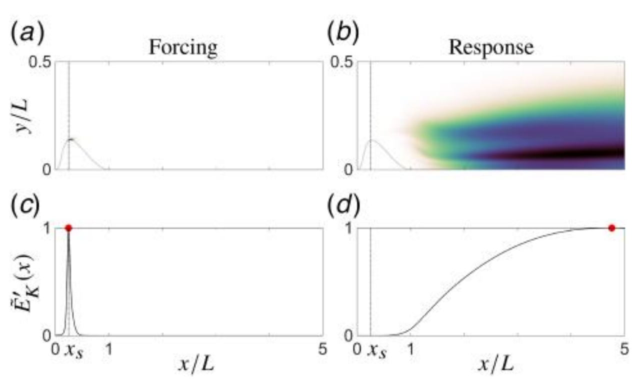

Fig. 2 (a), (b) Contours of the normalized kinetic energy $\tilde{E}'_K(x, y)$, and (c), (d) the streamwise distribution of its integrated form $\tilde{E}'_K(x)$, for $\mathrm{St}/\sqrt{\mathrm{Re}} = 0.006$. The response contours are normalized from 0 to 1, while the forcing contours are scaled from 0 to 0.1. The filled circular markers in panels (c), (d) indicate the peak values.

This maximal energy map shows a clear streamwise offset between the forcing and response maxima: the forcing peak occurs near the separation point and upstream of the recirculation bubble, along the wall of the hump, whereas the response peak remains downstream of the separation point, primarily within the separated shear layer at higher frequencies and extending into the wake region at lower frequencies. This streamwise offset between the forcing and response peaks indicates a predominantly convective disturbance mechanism, validating the causal direction identified experimentally by Celik et al. [6].

The optimal gain defined in Eq. (10) is a global measure incorporating both the rate of energy amplification and the spatial extent of the response to the forcing. Figure 5 shows the variation of the optimal gain with the scaled frequency in the dashed curve labeled *no-filter case*. The optimal gain reaches its maximum at $\mathrm{St}/\sqrt{\mathrm{Re}} = 0.006$, and the corresponding mode exhibits the large

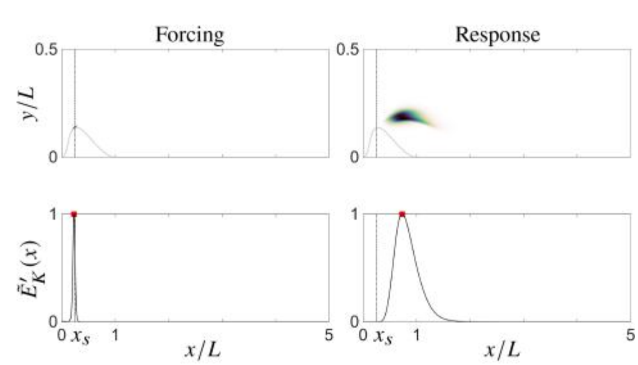

Fig. 3 Kinetic energy maps for $\mathrm{St}/\sqrt{\mathrm{Re}} = 0.035$. The notation is the same as Fig. 2, except that square markers indicate the peak values.

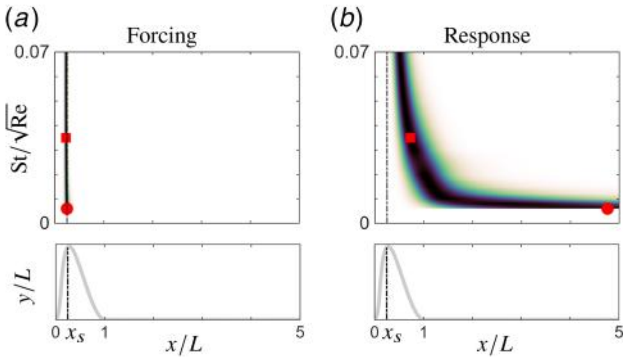

Fig. 4 Contour maps depicting the streamwise locations of the maxima of $\tilde{E}_K'(x)$, Eq. (14), as a function of frequency for the (a) forcing and (b) response modes, plotted above the shape of the hump for spatial reference. The circular and square markers indicate the peak locations corresponding to Fig. 2, at $\mathrm{St}/\sqrt{\mathrm{Re}} = 0.006$, and Fig. 3, at $\mathrm{St}/\sqrt{\mathrm{Re}} = 0.035$, respectively.

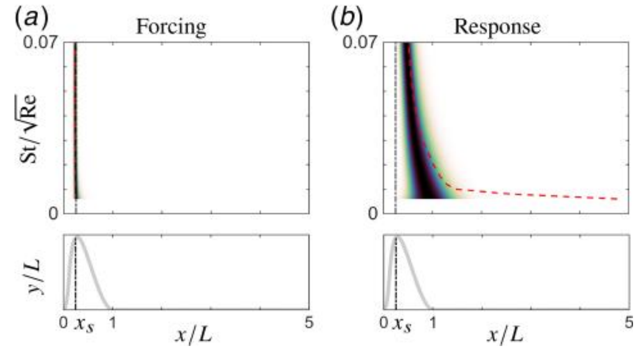

Fig. 6 Contour maps depicting the streamwise locations of the maxima of $\tilde{E}_K'(x)$, Eq. (14), as a function of frequency for the (a) forcing and (b) response modes, plotted above the shape of the hump for spatial reference. These maps highlight how temporal filtering shifts the streamwise position of the energy maxima, particularly for the response mode, compared with the unfiltered trends shown in Fig. 4(b). The peak contours from Fig. 4 are overlaid as dashed lines for reference.

downstream spatial extent characteristic of wake-dominated behavior, as shown in Fig. 2. However, such low frequency, wake-dominated modes may have limited practical relevance due to the fact that real systems experience temporal and spatial dissipation of input actuation and output responses. Therefore, we introduce temporal and spatial filters in the following sections to examine how temporal and spatial signal decays can influence the disturbance growth as measured by the optimal gain.

3.2 Temporal Filtering. The temporal filter is governed by an imaginary frequency parameter ω_i, which represents the frequency-domain counterpart of a temporal weighting, and thus indicates a temporal decay of the signals and may be selected based on the time horizon of physical interest, following the approach of Ref. [11]. Incorporating this filter leads to a discounted resolvent operator, obtained by shifting the temporal frequency in Eq. (9) by the decay rate ω_i. The resulting modified frequency-domain system now includes a complex frequency and is written as

$$(-\mathrm{i}(\omega_r + \mathrm{i}\omega_i)\mathbf{I} + \mathbf{J})\hat{\mathbf{q}} = \hat{\mathbf{f}} \tag{15}$$

The temporal filter effectively suppresses the contribution of long-time perturbations through exponential discounting, thereby highlighting dynamics that exhibit finite-time transient amplification. The temporal filter magnitude can be written non-dimensionally as a Strouhal number.

$$\mathrm{St}_{\omega_i} = \frac{\omega_i L}{u_\infty} \tag{16}$$

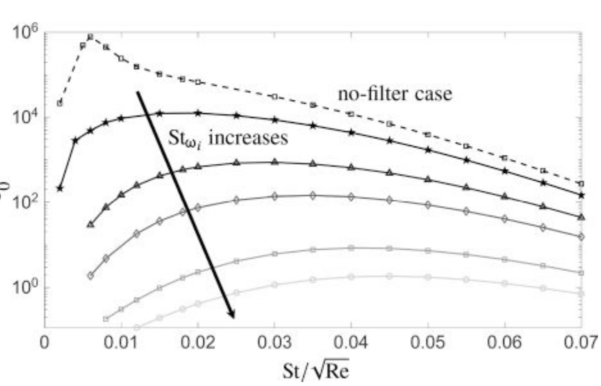

Fig. 5 Optimal gain versus scaled frequency for different temporal filters: $\mathrm{St}_{\omega_i}/\sqrt{\mathrm{Re}} = 0.0006, 0.002, 0.003, 0.006,$ and 0.008

In the present study, St_{ω_i} is chosen within a range of approximately −90% to +33% around the forcing frequency that corresponds to the maximum unfiltered gain, $\mathrm{St} \approx 0.006\sqrt{\mathrm{Re}}$.

The effect of temporal filtering on the optimal gain is shown in Fig. 5. Across all frequencies, the unfiltered case exhibits the largest gain, while the temporal filter reduces the optimal gain. Furthermore, the filtering shifts the energetic modes from the wake-dominated range to higher frequencies. The response-mode energy also shifts upstream, closer to the hump due to temporal filtering, as illustrated by a contour plot of the x-location of the maximum integrated kinetic energy in Fig. 6 (compare with Fig. 4).

The temporal filtering can therefore be used to adjust the decay of the forcing and response modes (refer to Fig. 14 in Appendix E). In practice, the filter values ($\mathrm{St}_{\omega_i}/\sqrt{\mathrm{Re}}$) are typically set to approximately an order of magnitude lower than the actuation frequencies of interest, following Ref. [11], and i.e., the range shown in Fig. 5. The ideal cutoff within this range is discussed in the comparison with experiments in Sec. 3.4.

In any case, the temporal filtering does not correct for the limited spatial extent over which experimental measurements are made. In the experiments of Ref. [6], wall-pressure measurements were used to assess the effect of acoustic forcing, and PIV measurements were acquired within a finite flow-field window to characterize its influence. Therefore, in the next section, we study the effect of spatial filters to emulate the limited spatial extent of the measurements. The filter is designed to place an increased weight near the wall surface, reflecting the wall-pressure measurement sensitivity and focusing the analysis on the near-wall dynamics of interest.

3.3 Spatio-Temporal Filtering. The spatial filtering of the response modes was performed by modifying the response matrix C from Eq. (6) with weights, W, based on the distance, D, of any given point in the domain, (x, y), from the wall, following Ref. [16], where the weighting function is defined as

$$W(x, y, d_c) = \frac{1-b}{2}\left[1 + \tanh\left(\kappa\frac{d_c - D(x,y)}{d_c}\right)\right] + b \tag{17}$$

with boundary conditions

$$\lim_{D\to 0} W = 1, \quad \lim_{D\to d_c} W = \frac{1+b}{2}, \quad \lim_{D\to\infty} W = b \tag{18}$$

The distance, D, is the minimum Euclidean distance to the wall; d_c is the cutoff distance (taken as a multiple of the vorticity thickness at the separation point, $\delta_{\mathrm{vort,s}}$); $b = 10^{-20}$ is the minimum weight to avoid numerical blow-up; and κ is chosen to satisfy the boundary values. The vorticity thickness at each wall point is computed along the local wall-normal line using the streamwise velocity defect and peak spanwise vorticity

$$\delta_{\text{vort}} = \frac{\bar{u}_e - \bar{u}_w}{\max|\bar{\Omega}_z|}, \qquad \bar{\Omega}_z = \frac{\partial \bar{v}}{\partial x} - \frac{\partial \bar{u}}{\partial y} \tag{19}$$

Figure 7 illustrates the spatial-filter regions corresponding to three different cutoff distances, $d_c = 7.5$, 15, and 20 $\delta_{\text{vort,s}}$. The cutoff values are chosen to obtain physically meaningful spatial domains. The minimum cutoff, $d_c = 7.5$, $\delta_{\text{vort,s}}$, illustrated by the innermost contour, is large enough to exceed the local vorticity thickness at every streamwise station along the hump (marked by the dot-dashed line) in order to isolate energetic shear-layer structures. The maximum cutoff, $d_c = 20$, $\delta_{\text{vort,s}}$, illustrated by the outermost contour, is roughly equal to the hump maximum thickness, and includes the full PIV window used in the experiments of Celik et al. [6] (shown by dashed square). This range ensures that the spatial filtering reflects the spatial extent over which optimal forcing and response can realistically be measured. The precise choice of cutoff within this range is explored in the comparison with experiments inSec. 3.4.

Applying these different spatial filters, in addition to the temporal filter $\text{St}_{\omega_i}/\sqrt{\text{Re}} = 0.002$, results in a modification of the optimal gain curves, shown in Fig. 8. The optimal gain rises with increasing spatial cutoff, with the unfiltered case yielding the highest gain, as expected. Moreover, spatial filtering shifts the most energetic frequency toward $\text{St}/\sqrt{\text{Re}} \approx 0.03 - 0.05$. The effect of the spatial filter on the resolvent mode shapes is illustrated with contour plots in Appendix F.

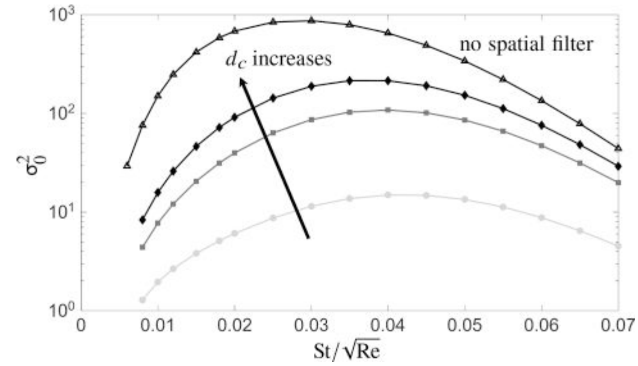

Fig. 8 Optimal gain as a function of frequency for the three spatial-filter levels, $d_c = 7.5$, 15, and 20 $\delta_{\text{vort,s}}$, illustrated in Fig. 7. All cases are evaluated using the same temporal filter, $\text{St}_{\omega_i}/\sqrt{\text{Re}} = 0.002$.

3.4 Comparison With Experimental Observations. Using both temporal and spatial filters for the resolvent operator, we can now make realistic comparisons between the predicted optimal gain of the resolvent analysis and a proxy for the optimal gain measured experimentally. Celik et al. [6] performed a forced-response study on the same hump geometry using acoustic actuation, combining time-resolved PIV and surface-pressure measurements to quantify how different forcing frequencies modified the lift coefficient. Their experiments showed that the lift response exhibits a strong frequency dependence, with a clear peak indicating the frequency range to which the flow is most receptive. Here, we normalized this lift coefficient variation, $\Delta C_L/\Delta C_{L,\max}$, and used it as a representation of the effectiveness of the forcing, i.e., the optimal response gain from the forcing, to compare with the normalized response gain predicted by the resolvent, $\sigma_0/\sigma_{0,\max}$.

Figure 9 compares the normalized response gain from the resolvent analysis, $\sigma_0/\sigma_{0,\max}$, with the experimentally measured normalized lift coefficient variation, $\Delta C_L/\Delta C_{L,\max}$ [6], using the previously defined spatial filter widths (maximum roughly equal to the hump thickness) and a temporal filter of $\text{St}_{\omega_i}/\sqrt{\text{Re}} = 0.002$, approximately an order of magnitude lower than the range of experimental actuation frequencies of interest, based on a similar cutoff used in Ref. [11]. The particular temporal cutoff frequency chosen within the range examined above corresponds to a time scale of approximately 0.017 s, which is close to the characteristic time scale of the flow, 0.013 s, calculated from the air-foil thickness (0.016 m) and friction velocity before separation ($0.07u_\infty$).

The optimal gain from the resolvent shows reasonably good agreement with the experimental lift proxy for the chosen temporal filtering, although the experimental curve exhibits a narrower and slightly shifted peak and a more rapid decay at higher frequencies. Different choices of temporal filtering tend to shift the peak without substantially modifying the width of the gain distribution. The spatial cutoff, on the other hand, primarily affects the high-frequency gain: larger cutoffs include more low-energy regions, diluting small-scale contributions and accelerating the decay, while smaller cutoffs retain the energetic small scales and sustain higher gains. Thus, the particular spatial cutoff chosen within the physically reasonable range explored above appears to have little effect on the experimental comparison.

The drop-off in experimental gain at high frequencies may be due to dissipative effects in the actual acoustic forcing resulting from nonlinear flow interactions that are not captured by the resolvent analysis. The resolvent analysis also relies on just the gain

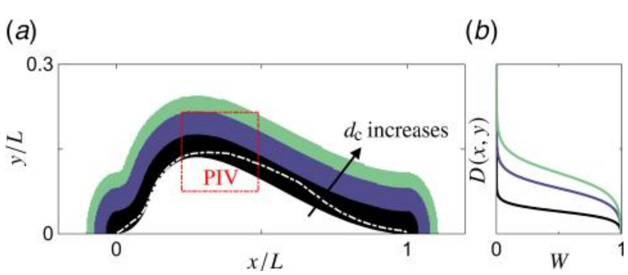

Fig. 7 Spatial weighting function: (a) contours of the cutoff distance, where the outermost boundary of each shaded region indicates the cutoff from the hump wall. The nested regions, from innermost to outermost, correspond to $d_c = 7.5$, 15, and 20 $\delta_{\text{vort,s}}$; the dot-dashed line marks the edge defined by the local vorticity thickness δ_{vort} at each streamwise location; and (b) one-dimensional profile of the Euclidean distance $D(x, y)$ of the grid points measured along the local wall-normal at the hump crest, plotted against the weighting function $W(D, d_c)$, for the same three cutoff distances..

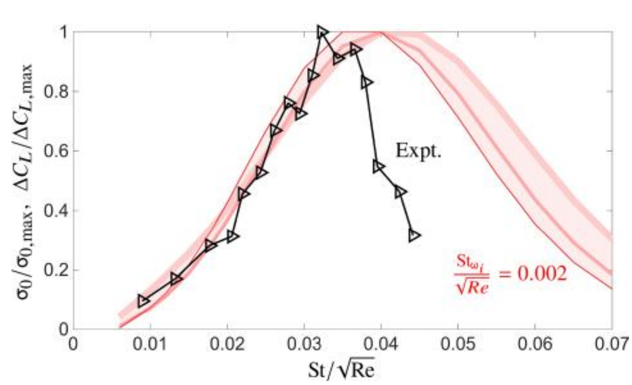

Fig. 9 Comparison of normalized experimental lift fluctuations $\Delta C_L/\Delta C_{L,\max}$ [6] and normalized resolvent gain $\sigma_0/\sigma_{0,\max}$ for temporally and spatially filtered modes. For the given $\text{St}_{\omega_i}/\sqrt{\text{Re}}$ value, the solid curves correspond to different spatial-filter cutoffs d_c, with line thickness decreasing as d_c increases. The cutoffs used are $d_c = 7.5$, 15.0, and 20.0 $\delta_{\text{vort,s}}$.

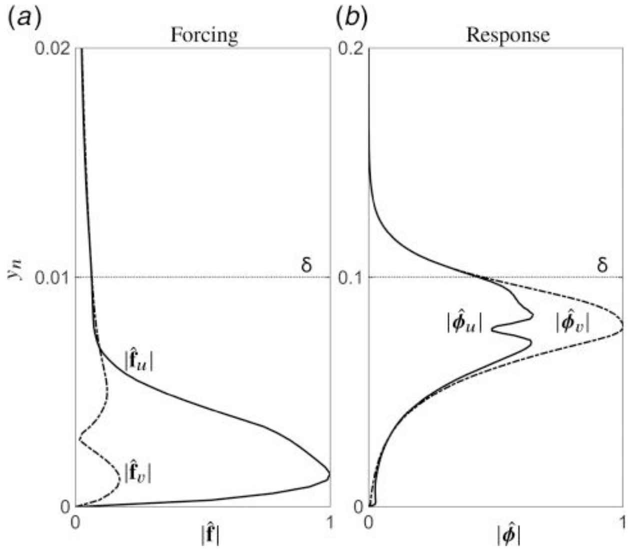

Fig. 10 Wall-normal profiles of the optimal (*a*) forcing and (*b*) response, evaluated at the streamwise locations corresponding to the maxima of integrated kinetic energy, Eq. (14). The forcing profile is shown at $x/L = 0.23$ and the response profile at $x/L = 0.50$, for $\mathrm{St}/\sqrt{\mathrm{Re}} = 0.040$, using filters with $\mathrm{St}_{\omega_i}/\sqrt{\mathrm{Re}} = 0.002$ and $d_c = 20.0\,\delta_{\mathrm{vort,s}}$.

from the most-amplified mode and does not allow for competing harmonics that may appear in the physical system. Finally, the lift coefficient variation may not be an ideal proxy for the overall energetic gain in the system, since some of the response energy will be distributed in changes in viscous and form drag. Despite these caveats, the resolvent appears capable of reasonable predictions of optimal actuation gains for the model high-lift airfoil.

The wall-normal profiles of the forcing and response velocity perturbations, evaluated at the streamwise location of maximum integrated energy (Eq. (14)), are shown in Fig. 10. The forcing profiles (left panel) indicate that the streamwise component is the most effective, with the forcing strongly concentrated near the wall. This can be qualitatively compared to the PIV observations reported in Ref. [6] of elongated near-wall structures in the attached boundary layer upstream of separation, which eventually organize the downstream shear layer. The response profiles (right panel in Fig. 10) show that the wall-normal velocity component becomes dominant, with the streamwise component of comparable magnitude. Both components attain their maxima near the boundary-layer edge, where the mean shear is the largest and the amplification mechanism is most active.

These results demonstrate the ability of resolvent analysis to identify the dominant forcing and response structures in the flow, providing a quantitative framework for understanding flow receptivity and amplification mechanisms. While the precise predictions depend on the selection of temporal and spatial filters, the results appear robust within a range of physically-motivated filter choices. The resolvent approach offers a versatile tool for diagnosing flow physics and guiding actuator placement or flow-control strategies. In this sense, resolvent analysis can serve as a design-oriented framework, enabling systematic exploration of flow modifications and optimization of control approaches before conducting costly experiments or high-fidelity simulations.

4 Conclusion

We performed resolvent analysis of the separated flow over a low-speed 2D hump model for a high-work-and-lift, low-Reynolds-number airfoil in order to show that the resolvent can identify the same mechanisms of disturbance amplification and receptivity previously found through experiments by Celik et al. [6]. We showed that two-dimensional modes are the most receptive; the optimal forcing mode is consistently located upstream of the separation bubble, near the wall, across all frequencies, while the response peaks downstream of the separation point, in the separated shear layer. The streamwise offset between the maxima of the integrated kinetic energy of forcing and response indicates a predominantly convective mechanism, consistent with the mechanism identified experimentally using correlation techniques. Temporal and spatial filtering was then applied to make optimal gain comparisons more physically relevant to experiments, and we showed that the normalized resolvent gain closely follows the experimentally measured lift-gain trend [6]. Qualitatively, the forcing modes exhibit a dominant streamwise velocity component with a peak near the wall, consistent with experimental observations of near-wall elongated structures, while the response modes attain their maximum near the boundary-layer edge, where the mean shear is the largest, reflecting the mechanism by which upstream wall modes organize the downstream shear layer. Together, these results validate the use of the 2D resolvent for predicting actuation response behavior on future high-work-and-lift, low-Reynolds-number airfoils.

Funding Data

- The US-Israel Binational Science Foundation (Grant No. 2022002).
- The Minerva Foundation (Grant No. AZ5746940764).

Conflict of Interest

There are no conflicts of interest.

Data Availability Statement

The datasets generated and supporting the findings of this article are obtainable from the corresponding author upon reasonable request.

Nomenclature

Greek Symbols

γ = specific heat ratio
δ = boundary-layer thickness
ν = kinematic viscosity
λ = wavelength
Ω = vorticity

Superscripts and Subscripts

e = boundary-layer edge value
s = separation point value
w = wall value
H = Hermitian transpose
vort = vorticity
∞ = freestream value

Dimensionless Groups

Pr = Prandtl number
Re = Reynolds number
St = Strouhal number

Appendix A: Baseflow—Solver Validation

The RANS flowfield, obtained using ANSYS FLUENT, was validated against the benchmark results of Ref. [12], and is shown in

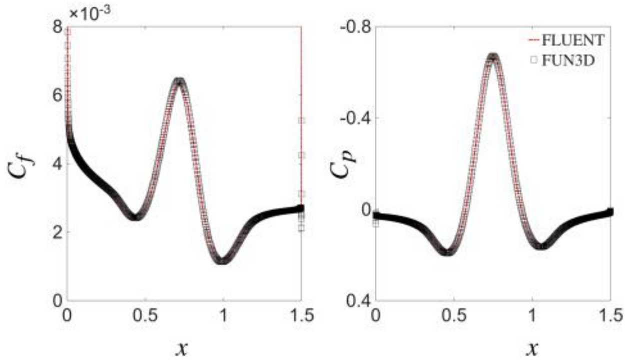

Fig. 11 Validation of the solver setup using the wall skin-friction coefficient C_f and wall pressure coefficient C_p. The FUN3D result is reproduced from the NASA bump benchmark [12]; both simulations use a 1409 × 641 grid.

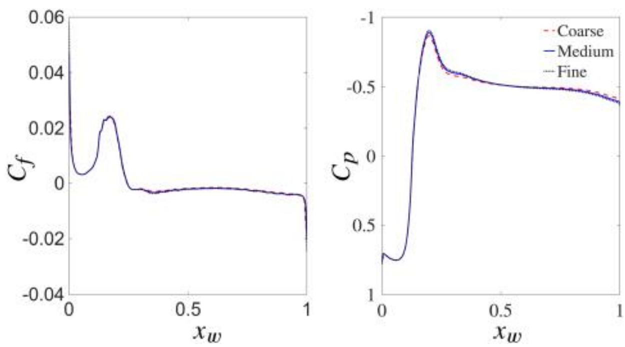

Fig. 12 Grid-independence assessment based on wall distributions of the skin-friction coefficient C_f and pressure coefficient C_p. The medium grid exhibits convergence and is chosen for the present study.

Fig. 11. The validated solver setup was then used to compute the baseflow for the present study, which serves as an input for the resolvent analysis.

Appendix B: Baseflow—Mesh Independence

The baseflow was checked for mesh independence to ensure that the resolvent analysis is insensitive to the grid resolution. The results for three levels of mesh refinement are shown with respect to the skin friction and pressure coefficients in Fig. 12.

Table 2 Streamwise locations of maximal forcing and response energy relative to the separation point x_s

$\mathrm{St}/\sqrt{\mathrm{Re}}$	$(\Delta x)_{\mathrm{forcing}}$	$(\Delta x)_{\mathrm{response}}$
0.006	−0.03	38.8
0.008	−0.07	20.1
0.010	−0.07	10.5
0.015	−0.07	7.9
0.020	−0.13	6.6
0.030	−0.13	4.8
0.040	−0.17	3.7
0.050	−0.20	3.0
0.060	−0.20	2.5
0.070	−0.17	2.3

Appendix C: Optimal Gain Contour

The frequency–wavenumber space of the optimal gain was scanned to identify the most amplified combination. As shown in Fig. 13(*a*), the two-dimensional disturbance (corresponding to n=0, where n denotes the number of discrete wavelengths in the spanwise direction) was found to be the most energetic and was therefore used in the subsequent analysis. Its forcing and response maps are shown in panel (*b*). The two most receptive modes after the two-dimensional mode are also illustrated in panels (*c*) and (*d*), for comparison.

Appendix D: Forcing-Response Peak Locations

Table 2 reports the streamwise locations of the maximal forcing and response energy relative to the separation point x_s for a range of forcing frequencies. Negative values of Δx indicate forcing peaks located upstream of separation, while positive values denote response peaks downstream of separation.

The data show that the forcing maximum remains clustered near and slightly upstream of separation, whereas the response maximum occurs progressively farther downstream at lower frequencies and moves closer to separation as frequency increases. This trend is consistent with convective amplification in the separated shear layer, where disturbances introduced upstream are amplified as they propagate downstream.

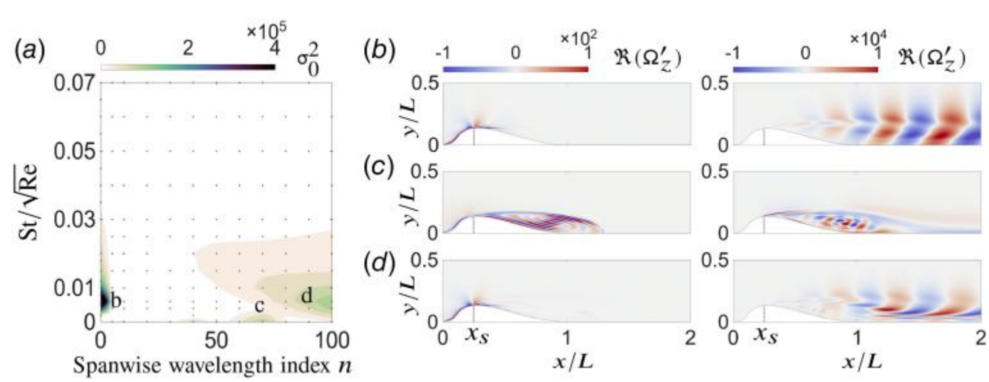

Fig. 13 (*a*) Optimal gain contours as a function of frequency and spanwise index n, where $\lambda_z = n\,\delta_{\mathrm{vort,s}}$ and $k_z = 2\pi/\lambda_z$. Gray dots denote the discrete points at which computations are performed, and values in between are obtained by linear interpolation. The markers (*b*)–(*d*) indicate three regions of the highest receptivity in frequency–wavenumber space. Panels (*b*)–(*d*) show the corresponding real part of spanwise-vorticity contours for representative modes from regions (*b*)–(*d*), respectively. Each panel contains both the forcing field $\hat{\mathrm{f}}$ on the left and the response field $\hat{\phi}$ on the right, (*b*) $n = 0$, $\mathrm{St}/\sqrt{\mathrm{Re}} = 0.006$, (c) $n = 70$, $\mathrm{St}/\sqrt{\mathrm{Re}} = 0$, and (*d*) $n = 100$, $\mathrm{St}/\sqrt{\mathrm{Re}} = 0.006$.

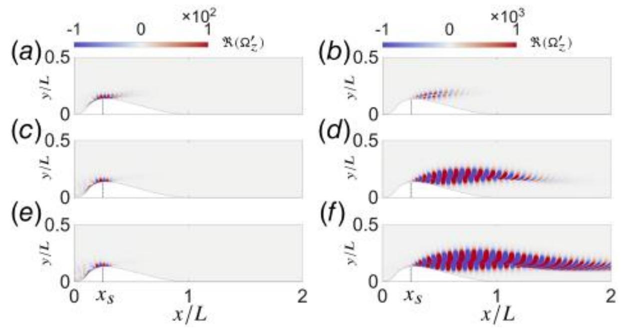

Fig. 14 Contours of the real part of the spanwise vorticity of the optimal modes at different temporal-filter levels, evaluated at $\mathrm{St}/\sqrt{\mathrm{Re}} = 0.040$. Panels (*a*), (*c*), (*e*) show the optimal forcing, while panels (*b*), (*d*), (*f*) show the corresponding optimal response. Panels (*a*), (*b*) correspond to $\mathrm{St}_{\omega_i}/\sqrt{\mathrm{Re}} = 0.008$, panels (*c*), (*d*) correspond to $\mathrm{St}_{\omega_i}/\sqrt{\mathrm{Re}} = 0.002$, and panels (*e*), (*f*) present the unfiltered case.

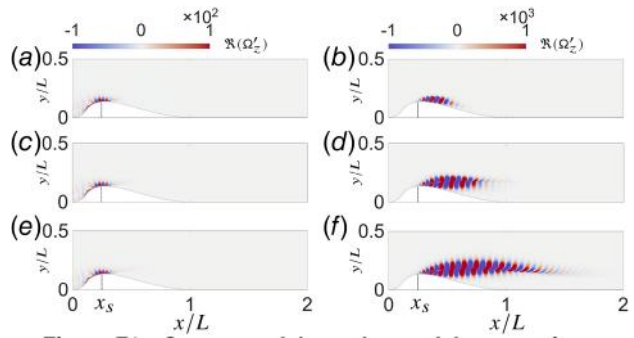

Fig. 15 Contours of the real part of the spanwise vorticity of the optimal modes at different spatial-filter levels. The effect of d_c on the spatial weighting function is shown in Fig. 7. Results are evaluated at $\mathrm{St}/\sqrt{\mathrm{Re}} = 0.040$ and $\mathrm{St}_{\omega_i}/\sqrt{\mathrm{Re}} = 0.002$. Panels (*a*), (*c*), (*e*) show the optimal forcing, while panels (*b*), (*d*), (*f*) show the corresponding optimal response. Panels (*a*), (*b*) correspond to $d_c = 7.5\,\delta_{\mathrm{vort,s}}$, panels (*c*), (*d*) correspond to $d_c = 20.0\,\delta_{\mathrm{vort,s}}$, and panels (*e*), (*f*) present the no-spatial-filter case.

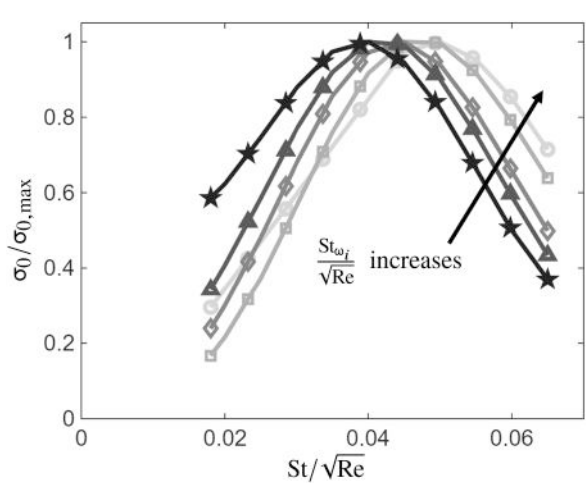

Fig. 16 Influence of temporal filtering on the leading resolvent gain. The normalized gain $\sigma_0/\sigma_{0,\max}$ is shown as a function of $\mathrm{St}/\sqrt{\mathrm{Re}}$ for temporal-filter cutoffs $\mathrm{St}_{\omega_i}/\sqrt{\mathrm{Re}} = 0.0006, 0.002, 0.003, 0.006$, and 0.008, computed at $\mathrm{Re} = 42{,}700$ and spatial cutoff $d_c = 20.0\,\delta_{\mathrm{vort,s}}$.

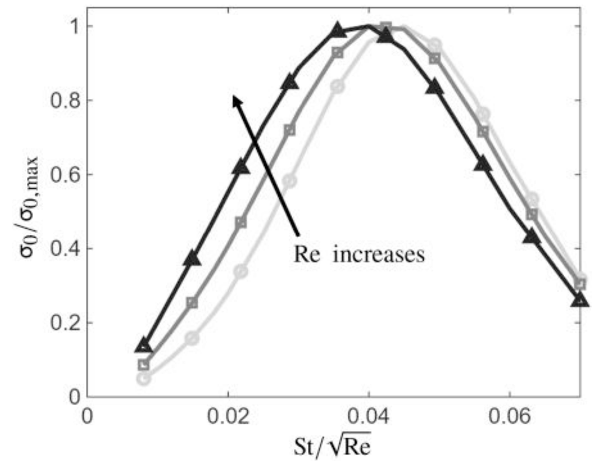

Fig. 17 Influence of Reynolds number on the leading resolvent gain. The normalized gain $\sigma_0/\sigma_{0,\max}$ is shown as a function of $\mathrm{St}/\sqrt{\mathrm{Re}}$ for $\mathrm{Re} = 39{,}000$, $42{,}700$, and $46{,}500$, computed at fixed forcing Strouhal number $\mathrm{St}_{\omega_i}/\sqrt{\mathrm{Re}} = 0.006$ and spatial cutoff $d_c = 20.0\,\delta_{\mathrm{vort,s}}$.

Appendix E: Effect of Temporal Filter

The spatial distribution of the resolvent modes as a function of the temporal filter choice is shown in Fig. 14, where moving down the rows illustrates how the modes change as the effect of temporal filtering decreases, approaching the unfiltered case.

Appendix F: Effect of Spatial Filter

The spatial filter assigns more weight near the wall and suppresses the modes away from the wall, toward its cutoff distance. The effect of different spatial filter cutoff distances the on the resolvent modes is shown in Fig. 15; only the response modes are affected by the spatial filtering.

Appendix G: Robustness of Resolvent Predictions to Temporal Filtering and Reynolds Number

Quantitatively, varying the temporal filter scale $t_b U/L$ by nearly an order of magnitude at fixed Reynolds number produces only moderate changes in the dominant response. The peak frequency shifts from about $f \approx 0.05$ to $f \approx 0.04$ (a $\sim 20\%$ decrease), while the response bandwidth—defined by the full width at half maximum of the gain curve—broadens by about 10–15%.

At fixed filtering parameters, varying the Reynolds number produces even smaller changes. The peak frequency remains clustered near $f \approx 0.04$, with variations below $\sim 10\%$, and the bandwidth increases by only about 10% over the Reynolds-number range considered.

Overall, these small percentage variations indicate that the dominant amplification frequency is robust, and that the response bandwidth exhibits only weak sensitivity to the filtering parameters and operating Reynolds number (Figs. 16 and 17).

References

[1] Clark, J., Paniagua, G., and Cukurel, B., 2024, "On the Development of High Lift, High Work Low-Pressure Turbines," ASME J. Turbomach., **146**(12), p. 121011.

[2] Seifert, A., Eliahu, S., Greenblatt, D., and Wygnanski, I., 1998, "Use of Piezoelectric Actuators for Airfoil Separation Control," AIAA J., **36**(8), pp. 1535–1537.

[3] Greenblatt, D., and Wygnanski, I. J., 2000, "The Control of Flow Separation by Periodic Excitation," Prog. Aerosp. Sci., **36**(7), pp. 487–545.

[4] Greenblatt, D., Goksel, B., Rechenberg, I., Schule, C. Y., Romann, D., and Paschereit, C. O., 2008, "Dielectric Barrier Discharge Flow Control at Very Low Flight Reynolds Numbers," AIAA J., **46**(6), pp. 1528–1541.

[5] Zhang, W., and Samtaney, R., 2015, "A Direct Numerical Simulation Investigation of the Synthetic Jet Frequency Effects on Separation Control of Low-Re Flow Past an Airfoil," Phys. Fluids, **27**(5), p. 055101.

[6] Celik, A., Mitra, A., Agarwal, T., Clark, J., Jacobi, I., and Cukurel, B., 2024, "Exploring Physics of Acoustic Flow Control Over Airfoils Toward Potential Application to High Work and Lift Turbines," ASME J. Turbomach., **146**(3), p. 031001.
[7] Celik, A., Mitra, A., Clark, J., and Cukurel, B., 2025, "Transonic Linear Cascade Demonstration of Acoustic Flow Control on High Work and Lift Turbines," ASME J. Turbomach., **147**(11), p. 111014.
[8] Rolandi, L. V., Ribeiro, J. H. M., Yeh, C. -A., and Taira, K., 2024, "An Invitation to Resolvent Analysis," Theor. Comput. Fluid Dyn., **38**(5), pp. 603–639.
[9] McKeon, B. J., Sharma, A., and Jacobi, I., 2013, "Experimental Manipulation of Wall Turbulence: A Systems Approach," Phys. Fluids, **25**(3), p. 031301.
[10] McKeon, B. J., Jacobi, I., and Duvvuri, S., 2018, "Dynamic Roughness for Manipulation and Control of Turbulent Boundary Layers: An Overview," AIAA J., **56**(6), pp. 2178–2193.
[11] Yeh, C.-A., and Taira, K., 2019, "Resolvent-Analysis-Based Design of Airfoil Separation Control," J. Fluid Mech., **867**, pp. 572–610.
[12] 2025, "SA Expected Results – 2D Bump-in-Channel Verification Case," NASA Langley Research Center, https://turbmodels.larc.nasa.gov/bump_sa.html, Accessed November 10, 2025.
[13] Dwivedi, A., 2020, "Global Input-Output Analysis of Flow Instabilities in High-Speed Compressible Flows," Ph.D. thesis, University of Minnesota, Minneapolis, MN.
[14] Bugeat, B., Chassaing, J.-C., Robinet, J.-C., and Sagaut, P., 2019, "3D Global Optimal Forcing and Response of the Supersonic Boundary Layer," J. Comput. Phys., **398**, p. 108888.
[15] Balay, S., Abhyankar, S., Adams, M., Brown, J., Brune, P., Buschelman, K., Dalcin, L., 2019, "PETSc Users Manual".
[16] Nogueira, P. A., Cavalieri, A. V., Hanifi, A., and Henningson, D. S., 2020, "Resolvent Analysis in Unbounded Flows: Role of Free-Stream Modes: PAS Nogueira et al.," Theor. Comput. Fluid Dyn., **34**(1), pp. 163–176.